Axion Dark Matter eXperiment around 3.3 μ eV with Dine-Fischler-Srednicki-Zhitnitsky Discovery Ability

C. Goodman, M. Guzzetti, C. Hanretty, L. J Rosenberg, G. Rybka, J. Sinnis, and D. Zhang* University of Washington, Seattle, Washington 98195, USA

John Clarke and I. Siddiqi University of California, Berkeley, California 94720, USA

A. S. Chou, M. Hollister, S. Knirck, and A. Sonnenschein Fermi National Accelerator Laboratory, Batavia, Illinois 60510, USA

T. J. Caligiure, J. R. Gleason, A. T. Hipp, P. Sikivie, M. E. Solano, N. S. Sullivan, and D. B. Tanner University of Florida, Gainesville, Florida 32611, USA

R. Khatiwada

Illinois Institute of Technology, Chicago, Illinois 60616, USA and Fermi National Accelerator Laboratory, Batavia, Illinois 60510, USA

G. Carosi, C. Cisneros, N. Du, N. Robertson, and N. Woollett Lawrence Livermore National Laboratory, Livermore, California 94550, USA

L. D. Duffy

Los Alamos National Laboratory, Los Alamos, New Mexico 87545, USA

C. Boutan, T. Braine, E. Lentz, N. S. Oblath, and M. S. Taubman Pacific Northwest National Laboratory, Richland, Washington 99354, USA

E. J. Daw, C. Mostyn, and M. G. Perry University of Sheffield, Sheffield S10 2TN, UK

C. Bartram

SLAC National Accelerator Laboratory, 2575 Sand Hill Road, Menlo Park, California 94025, USA

T. A. Dyson, S. Ruppert, and M. O. Withers Stanford University, Stanford, CA 94305, USA

C. L. Kuo

SLAC National Accelerator Laboratory, 2575 Sand Hill Road, Menlo Park, California 94025, USA and Stanford University, Stanford, CA 94305, USA

B. T. McAllister

Swinburne University of Technology, John St, Hawthorn VIC 3122, Australia

J. H. Buckley, C. Gaikwad, J. Hoffman, and K. Murch Washington University, St. Louis, Missouri 63130, USA

M. Goryachev, E. Hartman, A. Quiskamp, and M. E. Tobar University of Western Australia, Perth, Western Australia 6009, Australia (ADMX Collaboration)

(Dated: November 12, 2024)

We report the results of a QCD axion dark matter search with discovery ability for Dine–Fischler–Srednicki–Zhitnitsky (DFSZ) axions using an axion haloscope. Sub-Kelvin noise temperatures are reached with an ultra low-noise Josephson parametric amplifier cooled by a dilution refrigerator. This work excludes (with a 90% confidence level) DFSZ axions with masses between 3.27 to 3.34 μ eV, assuming a standard halo model with a local energy density of 0.45 GeV/cm³ made up 100% of axions.

Numerous cosmological and astrophysical observations provide compelling evidence for the existence of dark matter, contributing about 85% of the total mass in our universe [1–3]. Identification of dark matter is one of the outstanding problems in modern particle and astrophysics. While a number of particle candidates have been proposed for dark matter such as weakly interacting massive particles [4–6], fuzzy dark matter [7, 8] and sterile neutrinos [9–11], the QCD axion [12–14] is particularly well motivated.

The QCD axion is a consequence of a beyond-standardmodel U(1) symmetry introduced to solve the strong CP problem, which, additionally, could comprise some or all of the dark matter [12–14]. Measurements of the neutron electric dipole moment place an upper limit on the strong interaction CP violation phase $\theta < 5 \times 10^{-11}$ [15, 16]. A global axial $U(1)_{PQ}$ symmetry introduced by Peccei and Quinn [12] undergoes spontaneous symmetry breaking at a very high temperature T_{PQ} [16]. At temperatures lower than T_{PQ} , a pseudo Nambu-Goldstone boson, the so-called QCD axion, is produced. The mass of the QCD axion will be stabilized after the temperature cools to the QCD phase transition temperature ($\sim 200 \text{ MeV}$). If $T_{\rm PQ}$ is lower than the reheating temperature after the universe undergoes inflation, QCD axion mass between $\mathcal{O}(1 \,\mu\text{eV})$ and $\mathcal{O}(1 \,\text{meV})$ is strongly motivated [16].

The Axion Dark Matter experiment (ADMX) has been described in previous publications [17–23]. The axion haloscope was first proposed by Pierre Sikivie [24] to search for axion dark matter decay via the inverse Primakoff effect [25], stimulated by immersing the cavity in a strong magnetic field. The outgoing photon carries the rest-mass and kinetic energies of the axion. When the putative photons are on resonance with the cavity modes, the signal is enhanced by the quality factor of the resonator. The enhanced signal is extracted with an antenna and recorded through an ultralow noise radio frequency (RF) readout chain. Previous works have described ADMX's sensitivity to both axion coupling benchmark models: Kim-Shifman-Vainshtein-Zakharov (KSVZ) [17–20, 26, 27] and Dine-Fischler-Srednicki-Zhitnitskii (DFSZ) [21–23, 28, 29] over a range of potential axion masses.

In this Letter, we report the exclusion of the axionphoton coupling under the assumption that axions make up all of the dark matter from data collected by ADMX in 2022. We also include a discussion on the difference between reported exclusion bounds and discovery potential for haloscopes.

The 2022 run scanned from 792 to 807 MHz (3.27 to 3.34 μ eV axion mass) to extend the sensitivity reported in the previous run [23] to DFSZ coupled axions at nominal dark matter densities. The total science data taking spans 71 days with 60% live time.

TABLE I. Cold space temperatures during the previous run and this run. The 'attenuator' is the one closest to the cavity that contributes the most thermal noise off-resonance (Fig. 1).

Location	2021 run [mK]	2022 run [mK]
Attenuator	145	95
Cavity	300	130
JPA	150	135

The experimental hardware described in [23] was refitted with a number of cryogenic upgrades, including replacement of the stainless-steel supports between the 1 K temperature stage and the milliKelvin temperature stage with carbon fiber rods, improved thermal sinking of components, and additional vacuum space absorption pumping. These upgrades yielded reductions in the physical temperatures of the components given in Tab. I.

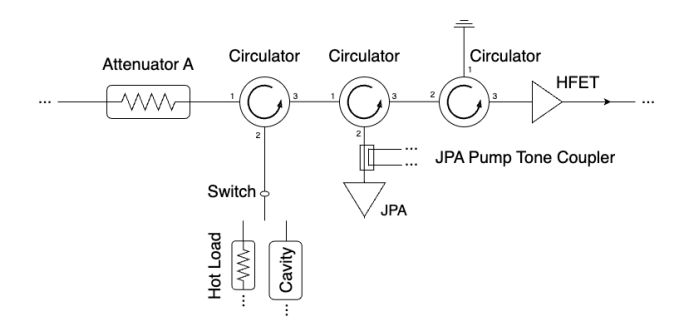


FIG. 1. A schematic of the RF components in the cold space. Other than HFET thermalized to the 4K plate, the components are at the milliKelvin temperature stage.

The signal power of the axion conversion extracted from the resonant cavity is

$$P_{a} = 2.8 \times 10^{-23} \text{W} \left(\frac{g_{\gamma}}{0.36}\right)^{2} \left(\frac{\rho}{0.45 \text{ GeV/cm}^{3}}\right)$$
$$\left(\frac{f}{800 \text{ MHz}}\right) \left(\frac{B}{7.6 \text{ T}}\right)^{2} \left(\frac{V}{106 \ell}\right) \left(\frac{C}{0.4}\right)$$
$$\left(\frac{Q_{L}}{45,000}\right) \left(\frac{\beta}{1+\beta}\right) \mathcal{L}(f, f_{0}, Q_{L}). \tag{1}$$

Here $g_{\gamma}=0.36~(-0.97)$ is a dimensionless coupling constant for the KSVZ (DFSZ) axion. The axion-to-two-photon coupling $g_{a\gamma\gamma}$ is $\alpha g_{\gamma}/\pi f_a$, where α is the fine structure constant, and f_a is the PQ symmetry breaking scale. The local dark matter density is noted as ρ . The photon frequency f corresponds to the total energy of the axion $f\approx m_a/h$ where m_a is the axion mass and h is the Planck constant. B is the average magnetic field in the cavity and $V=106~\ell$) is the volume excluding the two rods in the cavity. The form factor C describes the the field overlap between the fundamental mode used for the axion dark matter search and the external magnetic field. Q_L and β are the loaded quality

^{*} Correspondence to dzhang95@uw.edu

factor and coupling constant of the cavity, respectively. $\mathcal{L}(f, f_0, Q_L) = 1/(1+4(Q_L(f-f_0)/f)^2)$ is the Lorentzian profile of a cavity with resonant frequency f_0 .

The experiment sensitivity to axion-like signals is characterized by the signal-to-noise-ratio,

$$SNR = \frac{FP_a}{k_B T_{sys}} \cdot \sqrt{\frac{t}{b}}, \tag{2}$$

where F is the signal efficiency, $T_{\rm sys}$ is the system noise temperature, k_B is the Boltzmann constant, t is the integration time, b is the bandwidth of the measured noise power, Typical values are t=100 s, b=100 Hz for ADMX Run 1 [30].

As Eq. 2 demonstrates, sensitivity depends strongly on $T_{\rm sys}$, which is a combination of the thermal noise from the physical temperature of the cavity and RF components combined with electronic noise introduced by the amplification stages. The overall system noise temperature is $\bar{T}_{sys} = 0.48 \pm 0.05$ K for the data taken between 792 and 807 MHz. About half of $T_{\rm sys}$ is the added noise from the first stage Josephson Parametric Amplifier (JPA). The details of the noise calibration are in the supplemental material A [31] (see also references [30, 32, 33] therein).

The JPA is a nonlinear device that is biased to operate in a nearly linear manner over a limited range of input pump power levels. At too high a power, its gain will be compressed and the SNRI mismeasured too low. For some excitation powers its gain can be mismeasured to be too high due to nonlinear effects. JPA gain $G_{\rm JPA}$ was measured through both a cavity reflection and transmission measurement which differed in excitation power by about 10 dB. To ensure that we were operating in the linear regime, only data where the measured gains were consistent between reflection and transmission measurements were used for science analysis. The survived data presents $\bar{G}_{\rm JPA}=21\pm1~{\rm dB}.$

We follow the data taking procedure and analysis established in [23], where 100-second power spectra in the vicinity of the TM₀₁₀ mode are taken at each tuning rod position and combined to search for candidate axion dark matter signals. Due to the degraded cavity tuning system, we also developed specific data quality cuts for this run based on the uncertainties of Q_L and β which replace those used in [23] (see the supplemental material B [31] and references [20, 34–37] therein). The fractional systematic uncertainties in SNR are summarized in Tab. II.

The cold receiver transfer function (frequency-dependent gain) in each power spectrum is removed by a sixth-order Padé-approximant first, followed by a second round removal using the averaged residual receiver shapes. In detail, we group every 1000 Padé-fit filtered spectra by time stamps. Then, the averaged residual receiver shape includes 15% to 85% quantiles of the 1000 mean ranked in the same group, excluding spectra with transient interference and potential signals. The second receiver shape removal avoids mis-identifying the pile-up of the Padé fit residues as excesses during spectrum combination.

TABLE II. The fractional systematic uncertainties in the SNR. We updated the uncertainty budget for B^2VC from 3% [23] to 6 % to account for the possible misalignment between the rod and the cavity wall (see the supplemental material B [31]). Because each digitization has different uncertainties in Q_L , β and $T_{\rm sys}$, we report the median fractional uncertainty.

Name	Fractional uncertainties
$\overline{B^2VC}$	6%
$Q_L \text{ (median)}$	2%
$\beta/(1+\beta)$ (median)	1%
$T_{\rm sys}$ (median)	10%

The removal of the receiver transfer function reduces the SNR of axion candidates by about 20% (corresponding to F=0.8 in Eq. 2). We quantify the impact of this background removal procedure and subsequent analysis steps by injecting software synthetic signals into the unprocessed power spectra and measuring the detection efficiencies. This Monte Carlo process also confirms our stated confidence level (CL). The software synthetic signals are calibrated via an understanding of our system noise and cavity parameters including Q_L and β which are all monitored throughout data-taking with periodic measurements.

We evaluate the resultant flattened spectra for two signal distributions: a boosted Maxwell-Boltzmann (MB) distribution with dark matter density 0.45 GeV/cm³ [38–40], and the N-body simulated model presented in [41] with dark matter density 0.63 GeV/cm³. We apply the frequency-dependent signal shape, accounting for the Lorentzian cavity resonant enhancement, via an optimal filter on each power spectrum, and add the signal strengths weighted by uncertainties to form one grand spectrum with 100-Hz resolution [30]. The systematic uncertainties in the individual frequency bin powers are propagated according to the weights [42].

The resultant grand spectrum is searched for excesses above the noise (with definitions discussed below) that would indicate candidate axion signals. Our initial scan acquired sufficient data such that a DFSZ axion of the MB shape would have an expected SNR \geq 3.5. Bins that have either a 3σ excess or have power measurements greater than $P_{\rm DFSZ}-1.281\sigma$ where $\sigma=1/{\rm SNR}$ when $P_{\rm DFSZ}$ is normalized to 1 (see Fig. 2) are flagged as candidate signals [30]. At the nominal SNR, the latter criteria is more stringent, so that 90% of DFSZ-power axion-like signals will be flagged as axion candidates, but the former can be strong in cases where the SNR is larger than our minimum SNR requirement. Statistically 0.1% of noise bins are expected to be flagged as candidates with SNR = 3.5.

Proper flagging of candidate signals is tested with the injection of axion signal-shaped RF power into the cavity from a weakly coupled port using a system called the synthetic axion generator [43]. The analysis personnel are

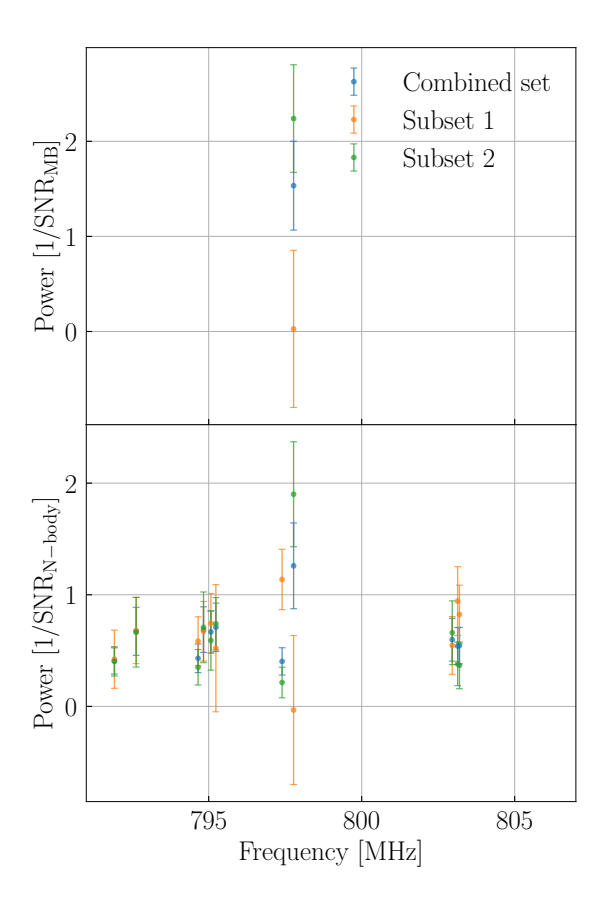


FIG. 2. SNR Normalized power of MB (top panel) and N-body (bottom panel) candidates with 3σ combined excess (blue). The two subsets (orange, green) power are overlain. The subset data with smaller SNR are preserved for impersistent candidates. The N-body case presents more candidates because the line-width of N-body axion dark matter is narrower, leading to a larger number of independent N-body axion dark matter candidates being scanned and more candidates statistically present as 3σ upper fluctuations.

blinded to the operation of the SAG during the initial round of data taking and the first re-scan. Synthetic signals are unblinded after the first re-scan, and the region is re-scanned with the signal turned off, and the signal is verified as having disappeared. All the synthetic signals were identified successfully and excluded with re-scans when the SAG was turned off during our data taking. Other than the SAG signals, we identified three persistent radio-frequency interference (RFI) signals. A signal coming from the cavity is maximized while on-resonance and follows the line-shape of the resonance, and the width of the signal strength is related to Q_L . Signals picked up by the receiver in components beyond the cavity will either have a strength independent of the cavity resonant frequency, or in some cases maximize only off-resonance of the cavity. Representative SAG and RFI signals are shown in Fig. 3, with features important to discrimination indicated. All the three persistent RFI signals are marked in Fig. 4 with gray dashed lines.

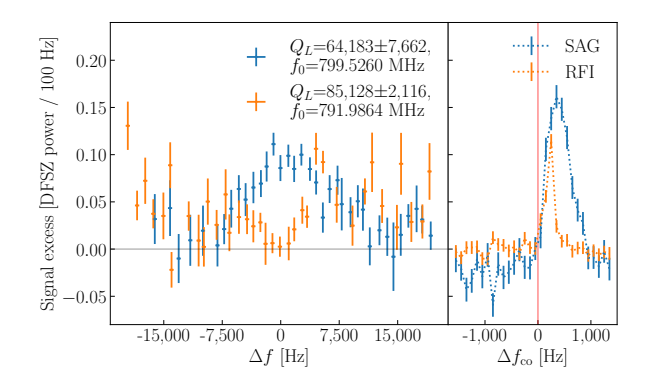


FIG. 3. A SAG signal (blue) found in the initial scan and a persistent RFI (orange) where f_0 is the candidate frequency and Δf shows the deviation from f_0 . Left: power excess per 100 Hz (receiver shape divided out) which takes the average of the power excess starting from the identified candidate frequency to 1 kHz beyond. We take the weighted average for the power spectra located in the same frequency bin [30]. Right: weight-summed power excess which is a zoomed-in version of the grand spectrum discussed in the text. Here, $\Delta f_{\rm co} = 0$ refers to the reference frequencies f_0 s (SAG only includes the initial scan, and RFI includes both the initial and re-scans). How the excesses change from off resonance to on resonance of the cavity is not included on the weight-summed power excesses (right) where the SAG and RFI are difficult to separate. However, if we group the power spectra according to the deviation to the cavity resonance, the grouped averaged power excesses (left) of the SAG are enhanced on resonance of the cavity and on the contrary, those of the RFI are reduced.

TABLE III. The number of candidates (with 100 Hz as the frequency resolution) not reaching to DFSZ 90% CL exclusion or presenting three sigma (3σ) excesses in this run and with previous data sets combined. All the 3σ excesses for both scenarios fail the persistence check as described below.

Distribution	This	Combined
MB (not reaching DFSZ)	3543	1181
N-body (not reaching DFSZ)	579	39
$MB(3\sigma)$	4	1
N-body (3σ)	19	11

Candidate signals are re-scanned—more power spectra are acquired within ± 3.5 kHz of the candidate frequency, and the persistence of the candidate is evaluated with the procedure defined in [30]. Typically enough integration time was spent on each candidate for a DFSZ signal to have a 4σ significance, thus clearly identifying signals and rejecting noise. We distinguish here between our upper bound on $g_{a\gamma\gamma}$ depicted in Fig. 4 as the exclusion limit, and the likelihood we would have successfully flagged and re-scanned a signal DFSZ axion at the nominal dark matter density (our discovery potential).

Re-scanned candidates that did not persist can be trivially eliminated as described in Ref. [23]. However, as a mechanical fault ended the data taking in the midst of the re-scan process, and some calibrations and adjustments

to analysis were done after the end of the run, there remained some regions of either insufficient sensitivity or un-rescanned 3σ excesses that needed to be addressed.

Data from this run were combined with the data from [22, 23] for computation of our overall sensitivity. Any regions still with insufficient sensitivity to exclude a DFSZ axion signal at 90% CL were treated as gaps in the data, and the local exclusion bounds were de-weighted accordingly. Frequency regions that still had a 3σ excess were examined for persistence by dividing the related spectra into two subsets with respect to timestamps as illustrated in Fig. 2. In all cases the two subsets were inconsistent with a persistent axion signal. These therefore can either be a transient or a statistical fluctuation. We used only the conservative subset with the lower SNR to set bounds on the axion-photon coupling, and do not exclude the possibility the excesses can be more prominent with higher SNRs. The effects of data combination are summarized in Tab. III.

As we had no persistent axion signal candidates, we interpreted the combined measured excess power in every bin as potentially due to an axion signal and computed the Frequentist upper limit at 90% CL as defined in Ref. [44] for each bin. These limits are smoothed for visualization in Fig. 4. Most bins exclude $g_{a\gamma\gamma}$ extensively below the level predicted for a DFSZ axion because we target SNR_{MB} = 3.5 in the initial data taking to have the ability to further study the gaps and potential signals. Since lower couplings would not have necessarily been flagged for re-scan, we claim a discovery potential of only 90% for DFSZ axion signals.

In summary, we set the most sensitive exclusion limits of $g_{a\gamma\gamma}$ with 90% CL as a function of the axion mass between 3.27 and 3.34 μ eV (Fig. 4), excluding the DFSZ axion as the dominant local dark matter with such masses with the same CL.

ACKNOWLEDGMENTS

We thank Jason Detwiler at University of Washington for discussions on the unbiased uncertainty estimator. Chelsea Bartram acknowledges support from the Panofsky Fellowship at SLAC. This work was supported by the U.S. Department of Energy through Grants No DE-SC0009800, No. DE-SC0009723, No. DE-SC0010296, No. DE-SC0010280, No. DE-SC0011665, No. DE-FG02-97ER41029, No. DE-FG02-96ER40956, No. DE-AC52-07NA27344, No. DE-AC03-76SF00098, No. DE-

SC0022148 and No. DE-SC0017987. Fermilab is a U.S. Department of Energy, Office of Science, HEP User Facility. Fermilab is managed by Fermi Research Alliance, LLC (FRA), acting under Contract No. DE-AC02-07CH11359. Pacific Northwest National Laboratory is a multi-program national laboratory operated for the U.S. DOE by Battelle Memorial Institute under Contract No. DE-AC05-76RL01830. University of Sheffield acknowledges the Quantum Sensors for the Hid-

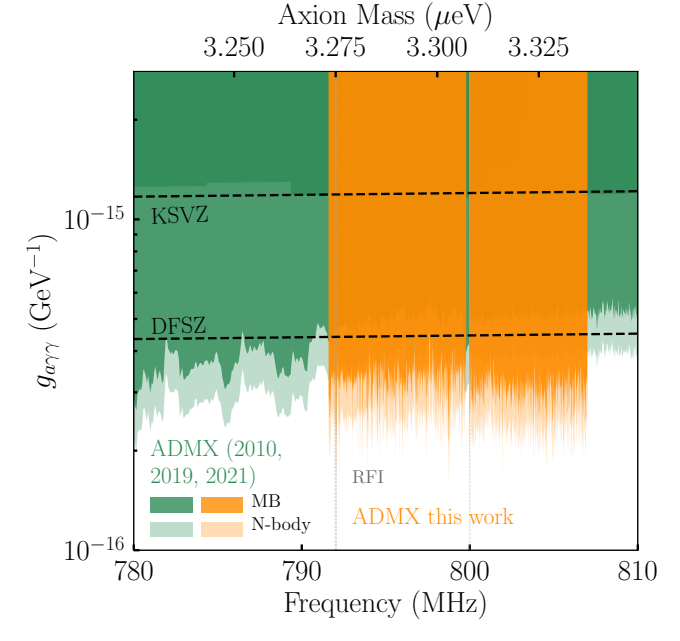


FIG. 4. The exclusion limits on $g_{a\gamma\gamma}$ with 90% CL of this work (orange shadow for the MB distribution and semi-transparent shadow for the N-body distribution). The previous ADMX searches with the same axion masses are overlain with dark green shadows [19], light green shadows [22, 23] for the MB distributions, and the semi-transparent green shadows [22, 23] for the N-body distributions. The RFIs are marked by the gray dashed lines. The two benchmark $g_{a\gamma\gamma}$ couplings (KSVZ and DFSZ) are marked with the black lines.

den Sector (QSHS) Extended Support under the grant ST/Y004620/1. UWA participation is funded by the ARC Centre of Excellence for Engineered Quantum Systems, Grant No. CE170100009, Dark Matter Particle Physics, Grant No. CE200100008, and Forrest Research Foundation. Additional support was provided by the Heising-Simons Foundation and by the Lawrence Livermore National Laboratory LDRD office.

^[1] F. Zwicky, Helvetica Physica Acta 6, 110 (1933).

^[2] V. C. Rubin and J. Ford, W. Kent, ApJ 159, 379 (1970).

^[3] Aghanim, N. et al. (Planck Collaboration), A&A 641, A6 (2020).

^[4] J. Aalbers *et al.* (LUX-ZEPLIN Collaboration), Phys. Rev. Lett. **131**, 041002 (2023).

^[5] E. Aprile *et al.* (XENON Collaboration), Phys. Rev. Lett. 131, 041003 (2023).

^[6] Y. Meng et al. (PandaX-4T Collaboration), Phys. Rev. Lett. 127, 261802 (2021).

^[7] L. Hui, J. P. Ostriker, S. Tremaine, and E. Witten, Phys. Rev. D 95, 043541 (2017).

- [8] W. Hu, R. Barkana, and A. Gruzinov, Phys. Rev. Lett. 85, 1158 (2000).
- [9] S. Dodelson and L. M. Widrow, Phys. Rev. Lett. 72, 17 (1994).
- [10] L. Canetti, M. Drewes, T. Frossard, and M. Shaposhnikov, Phys. Rev. D 87, 093006 (2013).
- [11] K. C. Y. Ng, B. M. Roach, K. Perez, J. F. Beacom, S. Horiuchi, R. Krivonos, and D. R. Wik, Phys. Rev. D 99, 083005 (2019).
- [12] R. D. Peccei and H. R. Quinn, Phys. Rev. Lett. 38, 1440 (1977).
- [13] S. Weinberg, Phys. Rev. Lett. 40, 223 (1978).
- [14] F. Wilczek, Phys. Rev. Lett. 40, 279 (1978).
- [15] C. Abel et al., Phys. Rev. Lett. 124, 081803 (2020).
- [16] F. Chadha-Day, J. Ellis, and D. J. E. Marsh, Science Advances 8, eabj3618 (2022).
- [17] S. Asztalos, E. Daw, H. Peng, L. J. Rosenberg, C. Hagmann, D. Kinion, et al., Phys. Rev. D 64, 092003 (2001).
- [18] S. J. Asztalos, R. F. Bradley, L. Duffy, C. Hagmann, D. Kinion, D. M. Moltz, et al., Phys. Rev. D 69, 011101 (2004).
- [19] S. J. Asztalos et al., Phys. Rev. Lett. 104, 041301 (2010).
- [20] J. Sloan *et al.*, Physics of the Dark Universe **14**, 95 (2016).
- [21] N. Du et al. (ADMX Collaboration), Phys. Rev. Lett. 120, 151301 (2018).
- [22] T. Braine et al. (ADMX Collaboration), Phys. Rev. Lett. 124, 101303 (2020).
- [23] C. Bartram *et al.* (ADMX Collaboration), Phys. Rev. Lett. **127**, 261803 (2021).
- [24] P. Sikivie, Phys. Rev. Lett. 51, 1415 (1983).
- [25] H. Primakoff, Phys. Rev. 81, 899 (1951).
- [26] J. E. Kim, Phys. Rev. Lett. 43, 103 (1979).
- [27] M. Shifman, A. Vainshtein, and V. Zakharov, Nuclear Physics B 166, 493 (1980).
- [28] M. Dine, W. Fischler, and M. Srednicki, Physics Letters B 104, 199 (1981).
- [29] A. P. Zhitnitskii, Sov. J. Nucl. Phys. (Engl. Transl.); (United States).
- [30] C. Bartram, T. Braine, R. Cervantes, et al. (ADMX Collaboration), Phys. Rev. D 103, 032002 (2021).
- [31] https://arxiv.org/pdf/2408.15227, supplemental Material.
- [32] Pulication in preparation.
- [33] J. Y. Mutus, T. C. White, R. Barends, Y. Chen, Z. Chen, B. Chiaro, A. Dunsworth, E. Jeffrey, J. Kelly, A. Megrant, et al., Applied Physics Letters 104, 263513 (2014).
- [34] M. T. Hotz, A SQUID-Based RF Cavity Search for Dark Matter Axions, Ph.D. thesis, University of Washington (2013).
- [35] J. Gurland and R. C. Tripathi, The American Statistician 25, 30 (1971).
- [36] C. Bartram, T. Braine, R. Cervantes, N. Crisosto, N. Du, G. Leum, P. Mohapatra, T. Nitta, L. J. Rosenberg, et al., Review of Scientific Instruments 94, 044703 (2023).
- [37] https://www.comsol.com.
- [38] M. S. Turner, Phys. Rev. D 42, 3572 (1990).
- [39] E. I. Gates, G. Gyuk, and M. S. Turner, The Astrophysical Journal 449, L123 (1995).
- [40] P. F. de Salas and A. Widmark, Reports on Progress in Physics 84, 104901 (2021).
- [41] E. W. Lentz, T. R. Quinn, L. J. Rosenberg, and M. J. Tremmel, The Astrophysical Journal 845, 121 (2017).

- [42] E. J. Daw, A Search for Halo Axions, Ph.D. thesis, Massachusetts Institute of Technology, Dept. of Physics (1998).
- [43] R. Khatiwada, D. Bowring, A. S. Chou, A. Sonnenschein, W. Wester, D. V. Mitchell, T. Braine, C. Bartram, R. Cervantes, N. Crisosto, et al., Review of Scientific Instruments 92, 124502 (2021).
- [44] P. D. Group, P. A. Zyla, et al., Progress of Theoretical and Experimental Physics 2020, 083C01 (2020).

Supplemental Material A: Noise Calibration

The characterization of the noise temperature $T_{\rm sys}$ is done through a two step process in this run. First, a Y-factor measurement of the second-stage Heterostructure Field Effect Transistor (HFET) amplifier yields the noise contribution of all components behind the first-stage JPA amplifier, $T_{\rm HFET}$. This is combined with the in-situ signal-to-noise-improvement (SNRI) measurement as described in detail in [30, 32], which is summarized here, because of its relevance to our more sophisticated treatment of the uncertainty.

During the Y-factor measurement of the HFET noise, the cryo-switch is connected to a thermal attenuator (hot load) instead of the cavity, and the pump tone of JPA is off. The noise power $P_{\rm HL}$ as a function of different physical temperature of the hot load $T_{\rm HL}$ is

$$P_{\rm HL} = G_{\rm total}bk_B(T_{\rm HL} + T_{\rm HFET}/\alpha),$$
 (A1)

where $G_{\rm total}$ is the total gain from the hot load to the digitizer. A fit of the power out of the receiver chain as a function of the hot load temperature is used to infer $T_{\rm HFET}/\alpha$, where α is the power transmissivity between the cavity reference and the HFET input. This transmissivity is mainly determined by the circulators. It should be noted that $T_{\rm HFET}/\alpha$ includes the noise contributed by the cables and electronics beyond the HFET, but these are a small contribution as long as the HFET gain is sufficiently large, as is the case here.

Two Y-factor measurements of the HFET, each over the entire frequency band, were made with a three-month separation. $T_{\rm HFET}/\alpha$ was calculated as a function of frequency by a linear interpolation, and the difference over time was included in the uncertainty. The measurements were consistent over time and yielded $T_{\rm HFET}/\alpha = 4.28 \pm 0.02$ K (4.00 ± 0.06 K) at 792 MHz (807 MHz).

The signal-to-noise-ratio improvement is

$$SNRI = \frac{G_{on}P_{off}}{G_{off}P_{on}},$$
 (A2)

where $G_{\rm on}$ ($P_{\rm on}$) and $G_{\rm off}$ ($P_{\rm off}$) are the gain (output power) with JPA pump tone on and off, respectively. These measurements are made every 5 to 10 digitizations and swept over a small bandwidth about the cavity resonance frequency and are also used to optimize the JPA gain.

When we compare the output powers with JPA pump tone on or off, the system noise temperature is

$$T_{\rm sys} = \frac{T_{\rm HFET}/\alpha}{{\rm SNRI}}.$$
 (A3)

Including the effects discussed, the overall system noise temperature is $\bar{T}_{sys} = 0.48 \pm 0.05$ K for the data taken between 792 and 807 MHz estimated by the SNRI method with $\bar{G}_{\rm JPA} = 21 \pm 1$ dB. Corrections to Eq. A3 due to the finite cavity temperature in addition to $T_{\rm HFET}/\alpha$ contribution in $P_{\rm off}$ in Eq. A2 during the SNRI measurement

are less than 2.5% and included in the noise uncertainty budget.

The noise power measurement varies noticeably with frequency on the scale of a single digitization bandwidth (Fig. 5), which becomes the dominant uncertainty in $T_{\rm sys}$ for most data. The bumps and asymmetries in the cold receiver shapes have two origins: (a) cavity-JPA standing wave interactions affecting the gain due to imperfect isolation provided by the circulators [33] and (b) the cavity temperature $T_{\rm cav}$ being higher than the offresonance noise temperature T_0 tracking the attenuator nearest to the cavity. For the configuration of the ADMX receiver in the operations reported here, the cavity-JPA interactions vary with changes to the JPA gain, and the two effects cannot be reliably separated, so they must be accounted for as an overall uncertainty on T_{sys} over the entire band digitized. The standard deviations in the cold receiver shapes are used as the systematic uncertainties in the noise power $P_{\rm on}$, which then propagate to $\sigma_{T_{\text{sys}}}$, the uncertainty on T_{sys} .

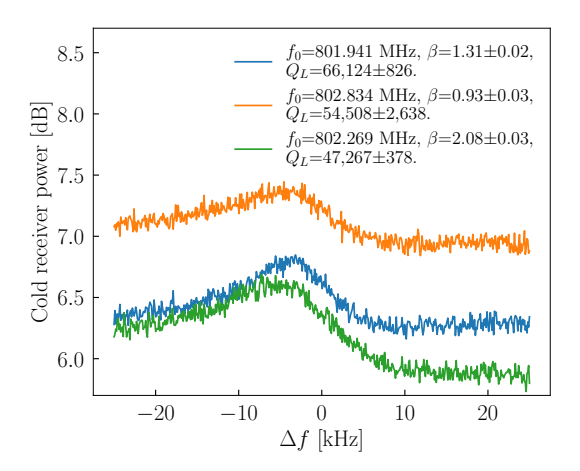


FIG. 5. Typical 50 kHz-wide cold receiver shapes with the room-temperature receiver shape removed (10 adjacent digitizations averaging for each). The center ($\Delta f = 0$) represents the center of the digitization at f_0 .

Supplemental Material B: Systematic Uncertainties

The cavity tuning system was somewhat degraded from the previous run. A mechanical issue appeared during the magnet ramp that caused unloaded quality factor Q_0 and antenna coupling β measurements to have periods of instability where rod motion could change Q_0 from measurement to measurement. This was also triggered by vibration during liquid helium fills to our reservoirs [20, 34]. Figure 6 illustrates a typical fluctuation of the loaded quality factor $Q_L = Q_0/(1+\beta)$ and β during the data taking. To characterize this anomalous behavior, we examine the averages and uncertainties of

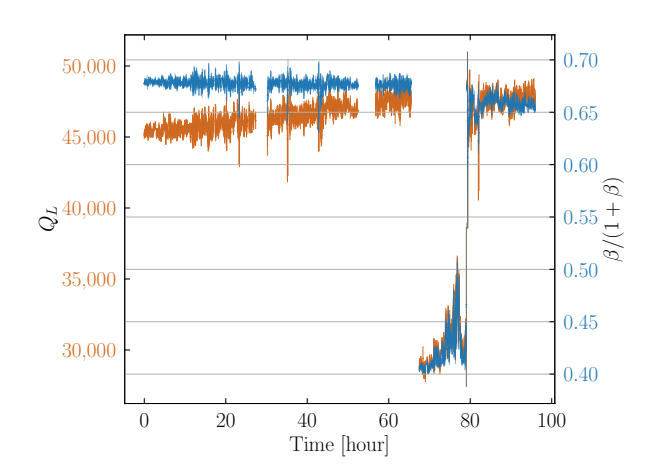


FIG. 6. A typical fluctuation of Q_L (red with axis on the left) and β (blue with axis on the right) during data taking due to mechanical instabilities.

TABLE IV. The fractions of the power spectra pass the quality cuts to remove digitizations with too large uncertainties in the related parameters. We apply all the cuts first and calculate the survival percentage of the power spectra with the cut under investigation removed. The survival percentages are similar under different cuts because most of the poor-quality data have unphysical values for all the critical parameters.

Cut removed	Percentage of the power spectra	
$\sigma_{Q_L}/Q_L < 17.7\%$	84.1%	
$\sigma_{\beta/(1+\beta)}/(\beta/(1+\beta)) < 21.6\%$	84.0%	
$\sigma_{T_{\rm sys}}/T_{\rm sys} < 34.2\%$	86.1%	
All applied	83.9%	

the N=4 nearest measurements of Q_L and β . The uncertainty estimator [35] of Q_L is

$$\sigma_{Q_L} = \sqrt{\frac{\sum_{i=1,N} (Q_{L_i} - \bar{Q}_L)^2}{N - 1.5}},$$
 (B1)

where \bar{Q}_L represents the average of the four Q_L measurements. A similar estimator is constructed for β . The uncertainties calculated in this way are propagated into the final uncertainties on axion power. Data with excessive Q_L or β uncertainties are excised from the data set.

We also studied the effect that the mechanical issues may have had on the form factor C. Since the resonant frequency of the cavity does not change more than $\mathcal{O}(1)$ kHz level while Q_L jumps, the change in Q_L does not cause significant change in C [36], which is verified by COMSOL multiphysics simulation [37] to be less than 1% while Q_L is dropped by a factor of 10. We also considered the potential misalignment between the cavity wall and the rod inside because we found the rods were stuck at some specific positions. We used the maximum allowed misalignment (1°) to estimate the uncertainties in C, which turns out to be 6% for this run. We included this updated form factor uncertainty in our final sensitivity limits.

We apply data quality cuts as listed in Tab. IV on the fractional uncertainties in Q_L and $\beta/(1+\beta)$ to reject mechanically unstable periods and on $T_{\rm sys}$ to reject possible erroneous gain measurements leading to large uncertainties of $T_{\rm sys}$. Outliers three-standard-deviation above the median of the fractional uncertainties are cut for both Q_L and $\beta/(1+\beta)$, and two-standard-deviation is used for $T_{\rm sys}$. A stronger quality cut on $T_{\rm sys}$ is applied to avoid the final SNR carrying large uncertainties.